Solar-Driven Photoelectrochemical Probing of Nanodot/Nanowire/Cell Interface

Jing Tang,[†] Yueyu Zhang,[‡] Biao Kong,[†] Yongcheng Wang,[†] Peimei Da,[†] Jun Li,[†] Ahmed A. Elzatahry,[⊥,∇] Dongyuan Zhao,[†] Xingao Gong,*[,‡] and Gengfeng Zheng*[,†]

[†]Laboratory of Advanced Materials, Department of Chemistry, Fudan University, Shanghai, 200433, China

[‡]Key Laboratory of Computational Physical Sciences, Ministry of Education, State Key Laboratory of Surface Physics, and Department of Physics, Fudan University, Shanghai, 200433, China

[⊥]Department of Chemistry, King Saud University, P.O. Box 2455, Riyadh 11451, Riyadh, Saudi Arabia

[∇]Polymer Materials Research Department, Advanced Technology and New Materials Research Institute, New Borg El-Arab City, P.O. Box 21934, Alexandria, Egypt

S Supporting Information

ABSTRACT: We report a nitrogen-doped carbon nanodot (N-Cdot)/TiO_2 nanowire photoanode for solar-driven, real-time, and sensitive photoelectrochemical probing of the cellular generation of H_2S, an important endogenous gasotransmitter based on a tunable interfacial charge carrier transfer mechanism. Synthesized by a microwave-assisted solvothermal method and subsequent surface chemical conjugation, the obtained N-Cdot/TiO_2 nanowire photoanode shows much enhanced photoelectrochemical photocurrent compared with pristine TiO_2 nanowires. This photocurrent

increase is attributed to the injection of photogenerated electrons from N-Cdots to TiO_2 nanowires, confirmed by density functional theory simulation. In addition, the charge transfer efficiency is quenched by Cu^{2+}, whereas the introduction of H_2S or S^{2-} ions resets the charge transfer and subsequently the photocurrent, thus leading to sensitive photoelectrochemical recording of the H_2S level in buffer and cellular environments. Moreover, this N-Cdot-TiO_2 nanowire photoanode has been demonstrated for direct growth and interfacing of H9c2 cardiac myoblasts, with the capability of interrogating H_2S cellular generation pathways by vascular endothelial growth factor stimulation as well as inhibition.

KEYWORDS: photoelectrochemical, nanowire, carbon nanodot, nitrogen-doping, H_2S
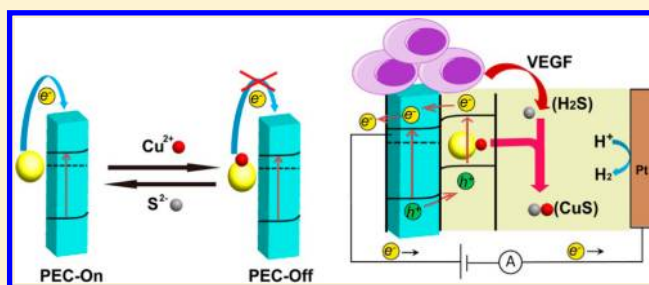
Real-time detection of trace physiologic messenger molecules, such as nitric oxide,[1] carbon monoxide,[2] and hydrogen sulfide[3] from cells and tissues, is important for studying fundamental cellular functions, disease diagnosis and medical treatment.[4−6] Among these endogenous gasotransmitters, hydrogen sulfide (H_2S) has been gaining substantial increase of recognition for its physiological role in regulating cardiovascular, neuronal, and immune functions.[7] The production of H_2S in mammals involves enzymes such as cystathionine γ-lyase (CSE), cystathionine-β-synthase, and 3-mercaptopyruvate sulfurtransferase.[8−10] Several methods have been demonstrated to detect H_2S or other physiologic messenger molecules in biological environments.[11−15] Nonetheless, due to the low concentration and relatively short lifetime of these signaling molecules near cells,[1] it is highly challenging to monitor the production and concentration of physiological H_2S in real time. Nanowire-based photoelectrochemical (PEC) biomolecule detection is a recently developed sensing approach that represents several unique features.[16−19] First, the semiconductor nanomaterial-based PEC conversion is capable of combining low intensity light source

(such as sunlight) and low electric field for generation of reactive charge carriers and photocurrent, thus enabling the targeted electrochemical reactions without inducing other possible side reactions. Second, the signal excitation and detection are based on light and electricity, thus effectively reducing the background noise.[19] Third, the light is absorbed along the nanowire's (NW's) micrometer-long axial direction, while the charges are separated and transported toward the radial direction to the NW surface for subsequent electrochemical reactions, leading to efficient PEC activity.[20] Fourth, the evolution of oxygen or other reactive oxidative species can diffuse into the interiors of bulky biomolecules and offer charge relay,[17] leading to efficient signal transducing that is challenging for conventional electrochemical methods where reactions only take place on the electrode surfaces.

Among the semiconductor materials being intensively investigated for the solar energy-driven PEC conversion and
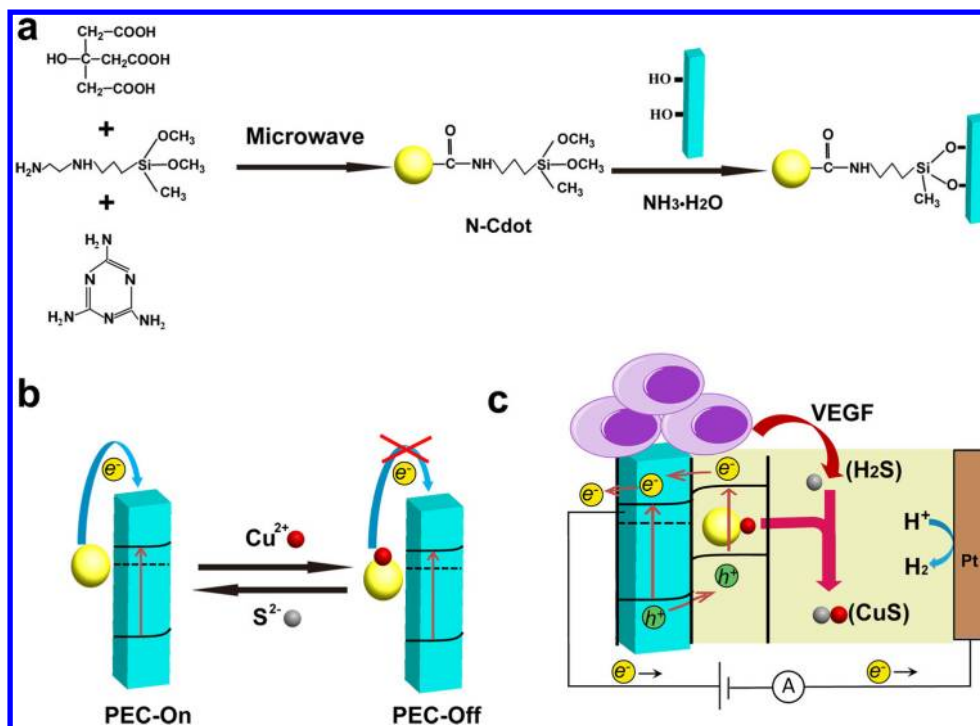
Figure 1. (a) Synthesis of N-Cdots and N-Cdot-TiO$_2$ NWs. (b) Transfer and tuning of photogenerated electrons between N-Cdots and TiO$_2$ NWs upon the addition of Cu^{2+} and S^{2-}, resulting in the PEC-off and PEC-on states, respectively. (c) PEC detection of H$_2$S by N-Cdot-TiO$_2$ NW PEC sensors interfaced with living cells. VEGF is added to the cell culture to generate H$_2$S, which combines with Cu^{2+} and reinstate the charge carrier transfer and the PEC current.
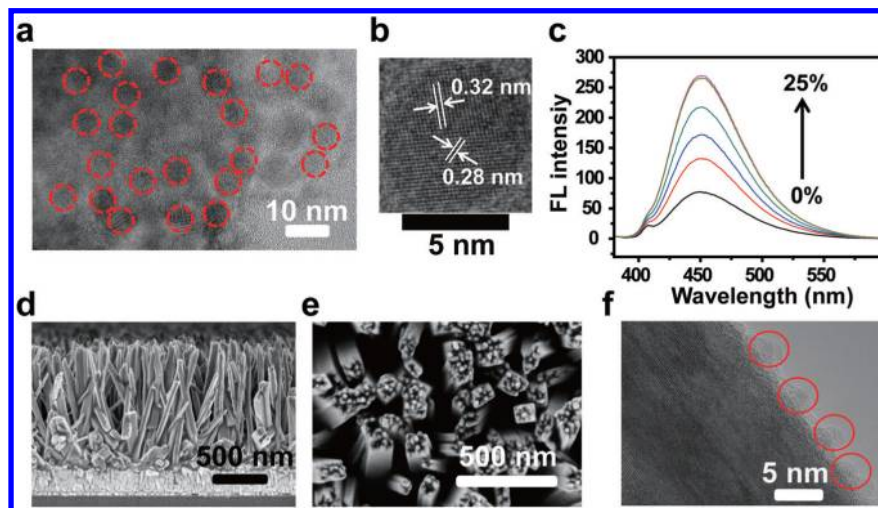

Figure 2. (a, b) HRTEM images of as-grown N-Cdots. (c) Fluorescence spectra of N-Cdots with different N-doping concentrations. (d) Side-view and (e) top-view SEM images of N-Cdot-TiO$_2$ NW arrays grown on a fluorine-doped tin oxide glass substrate. (f) TEM image of a representative N-Cdot-TiO$_2$ NW. The positions of N-Cdots on the TiO$_2$ NW surface are highlighted by red circles.

water splitting,[21] TiO$_2$ has been demonstrated as one of the most attractive candidate for PEC sensing, due to its high stability, favorable band edge position, reasonable charge transport kinetics, facile surface functionalization, and environment benignity.[22−24] Nonetheless, a well-known deficiency of TiO$_2$ is its large band gap (E_g = 3.0−3.2 eV), which limits its absorption mainly in the UV range.[20,25−27] Thus, a number of approaches have been reported for TiO$_2$ sensitization with small band gap semiconductors to enhance the photoabsorption and PEC activity.[28,29] In particular, carbon nanodots (Cdots), synthesized by electrodeposition[30] or hydrothermal methods,[31] have recently been reported for surface adsorption

and sensitization of TiO$_2$. However, the PEC efficiency is still suboptimal due to the limited quantum efficiency of Cdots.[32] Meanwhile, the heterostructures from physical adsorption of Cdots on TiO$_2$ surface results in low stability, and thus, it is challenging to serve as a robust PEC sensing platform with stable cellular interface, as well as sensitive and selective in situ electrochemical monitoring of cellular physicochemical activities.

In this paper, we developed a nanomaterial−cell platform composed of nitrogen-doped Cdots (N-Cdots)/TiO$_2$ NWs and H9c2 cardiac myoblasts, which allowed for real-time probing of physiological levels of H$_2$S messenger generated by living cells,
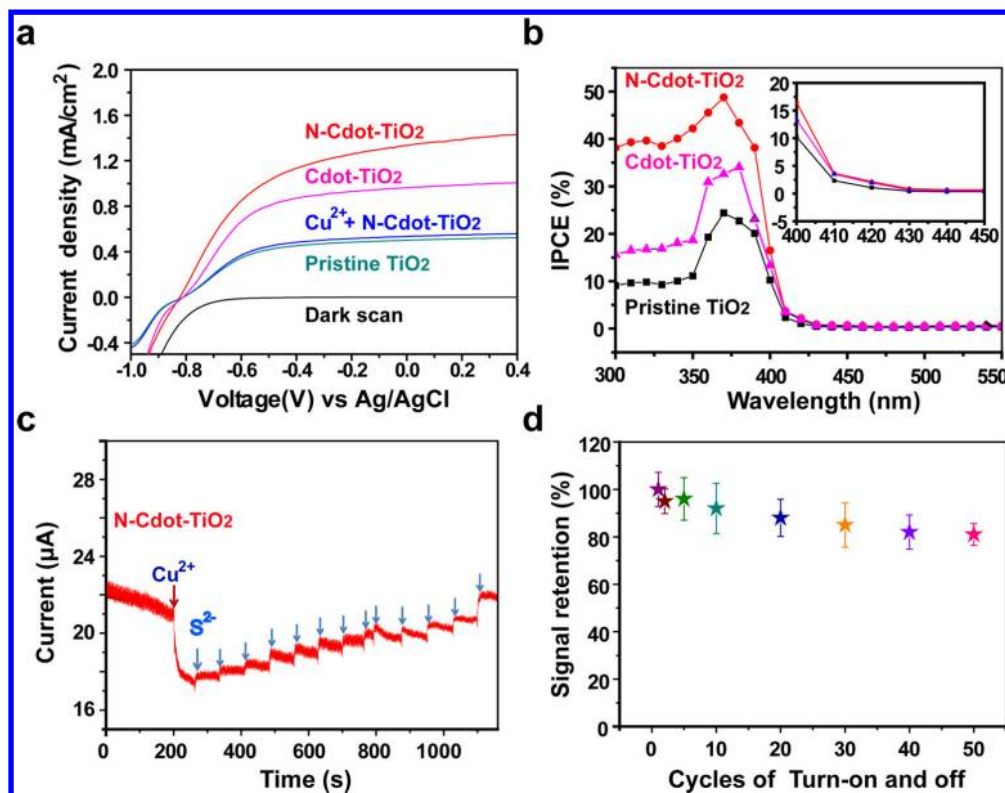
Figure 3. PEC measurement and sensing. (a) Linear sweep voltammograms measured from the pristine TiO_2 NWs (curve 1), Cdot-TiO_2 NWs (curve 3), N-CDot-TiO_2 NWs (curve 4), and N-CDot-TiO_2 NWs incubated with Cu^{2+} (curve 2). The dark current of the N-CDot-TiO_2 NWs (black curve) is also plotted for comparison. (b) IPCE curves of the pristine TiO_2 NWs (black curve), Cdot-TiO_2 NWs (pink curve), and N-Cdot-TiO_2 NWs (red curve). Inset: magnification of the IPCE spectra in the wavelength range of 400−450 nm. (c) Photocurrent versus time data of a N-Cdot-TiO_2 NW biosensor for successive addition of Cu^{2+} (1 μM, red arrow) and S^{2-} (with a final concentration increase from 10 to 100 nM each time, blue arrows) into a phosphate buffer (pH 7.4) at 0 V vs Ag/AgCl under 100 mW cm^{-2} of simulated sunlight illumination. The size of the active sensor area was 0.02−0.06 cm^2, defined by epoxy sealing. (d) Signal retention stability of a N-Cdot-TiO_2 NW PEC sensor upon the repeated addition of Cu^{2+} and S^{2-}, that is, the cycles between the PEC-on and PEC-off states.

based on an interfacial charge carrier transfer and tuning mechanism. The N-Cdots are first synthesized by a microwave-assisted solvothermal growth, followed by covalent attachment onto TiO_2 nanowire (NW) surface via a facile silane-coupling chemistry (Figure 1a). The efficient nitrogen doping leads to a much enhanced and stable fluorescence compared to undoped Cdots, allowing for increased transfer of photogenerated electrons toward TiO_2 NWs and, subsequently, much higher photocurrent (i.e., the PEC-on state) than pristine (unfunctionalized) TiO_2 NWs. This charge transfer from Cdots and TiO_2 NWs increase can be inhibited by the existence of copper ion (Cu^{2+}) near NW sensor surfaces due to transferring of photogenerated electrons from the excited states of N-Cdots to the d orbitals of Cu^{2+}, resulting in the photocurrent reduction to the level of pristine TiO_2 NWs (i.e., the PEC-off state) (Figure 1b). Further introduction of H_2S or S^{2-} ions can competitively bind to Cu^{2+} and reinstate the transfer of photogenerated electrons to the PEC-on state, indicating an interfacial charge carrier transfer and tuning scheme. The detection sensitivity of H_2S has reached 10 nM in buffer, among the best of the previously reported H_2S sensors.[14,15] Furthermore, H9c2 cardiac myoblasts directly grown on and interfacing to the N-Cdot-TiO_2 NWs are used for real-time monitoring of the H_2S generation upon the vascular endothelial growth factor (VEGF) excitation and different cellular inhibition pathways (Figure 1c), suggesting the capability of

studying the nanomaterial-cell interfaces by the N-Cdot-TiO_2 NW PEC sensors.

The N-Cdots were synthesized by a microwave-assisted one-pot solvothermal growth method, in which citric acid and melamine were used as the carbon and nitrogen sources, respectively, and N-(β-aminoethyl)-γ-aminopropyl methyldimethoxysilane (AEAPMS) was used as both the solvent and the capping agent. After the synthesis, the N-Cdots are well dispersed in aqueous solution without noticeable aggregation. Atomic force microscopy (AFM) images show that most of the as grown N-Cdots have an average diameter of ∼4−7 nm, and remain as individual particles when deposited onto substrates (Supporting Information Figure S1). High-resolution transmission electron microscopy (HRTEM) images (Figure 2a, b) of these N-Cdots exhibit well-resolved lattice fringes with d-spacings of 0.28 and 0.32 nm, corresponding to the (020) and (002) planes of graphitic carbon, respectively.[33,34] The in situ nitrogen doping of the Cdots is confirmed by the X-ray photoelectron spectroscopy (XPS), which displays a distinct peak at 398.8 eV (Supporting Information Figure S2) attributed to the N 1s binding energy of the C−N bond.[34]

The UV−vis spectra of the as-synthesized N-Cdots show an absorption peak centered at ∼360 nm in the range of 300−550 nm, in which the peak intensity increases with the increase of the N doping ratio (Supporting Information Figure S3). The photoluminescence (PL) spectra of the as-grown N-Cdots are then measured by excitation at 360 nm, which exhibit strong

blue PL intensity and a sharp peak centered at ~455 nm (Figure 2c), consistent with recent reports on nitrogen-doped carbon nanoparticles synthesized by a hydrothermal method.[35] The enhanced fluorescence property of the N-Cdots is further investigated at the 450 nm emission peak. The fluorescence quantum yield measurement show that the N-Cdots and undoped Cdots have quantum yields of 41% and 35%, respectively, further indicating that both the fluorescence lifetime and quantum yield of the Cdots are substantially increased by the in situ nitrogen doping. The N-Cdots possess stable photostability for over six months with a transparent appearance and strong blue color under UV light (Supporting Information Figure S4) as well as showing low cytotoxicity for cells (Supporting Information Figure S5), suggesting their excellent potential for interfacing of cells and long-time cellular measurement.

The N-Cdots are further covalently conjugated to the hydrothermally grown TiO_2 NW surface via the surface silane molecules, which are covalently linked during the one-pot microwave-assisted synthesis step. Scanning electron microscopy (SEM) images show that the N-Cdot-TiO_2 NW arrays are uniform and normally grown from the growth substrate, with the average length and diameter around 1.5−2 μm and 100−150 nm, respectively (Figure 2d, e). TEM images show that each TiO_2 NW is single-crystalline, and the surface is covered by a thin layer of particles with average diameters of ~5 ± 2 nm (Figure 2f). The elemental mapping of a representative N-Cdot-TiO_2 NW shows uniform distribution of the C, N, and Si signals over the entire NW (Supporting Information Figure S6), suggesting the successful silane linkage of the N-Cdots over the TiO_2 NWs. Fourier transform infrared (FTIR) spectra of the N-Cdot-TiO_2 NWs exhibit several distinct bands centered at 3435, 2926, 1658, 1251, 1092, and 798 cm^{-1} (Supporting Information Figure S7, red curve), which are attributed to O—H, C—H, C＝O, N—H, C—N, and C—O peaks.[36] These peaks are similar to those measured from the N-Cdots (Supporting Information Figure S7, blue curve), confirming the covalent binding of N-Cdots on TiO_2. In addition, the strong intensity of the carbonyl and hydroxyl peaks suggest the excellent hydrophilic property and water solubility of the silane-functionalized N-Cdots, which benefits for further Cu^{2+} coupling.[37]

The PEC biosensing capability of the N-Cdot-TiO_2 NWs is first investigated by the photocurrent measurements in a three-electrode PEC cell at pH 7.4, with the absence of the molecular targets. Under 100 mW cm^{-2} of simulated sunlight, the photocurrent density of the N-Cdot-TiO_2 NW photoanode reaches ~1.33 mA cm^{-2} at 0 V vs Ag/AgCl (or 0.6 V vs reversible hydrogen electrode, RHE), substantially higher than the photocurrent values of the pristine TiO_2 NWs and the Cdot-TiO_2 NWs (0.51 and 0.96 mA cm^{-2}), respectively (Figure 3a). The incident-photon-to-current conversion efficiency (IPCE) values of the pristine TiO_2 NWs and the Cdot-TiO_2 NWs are about 10−20% and 20−35%, respectively, in the range of 300−400 nm (Figure 3b). In contrast, the N-Cdot-TiO_2 NWs show a much enhanced IPCE value of 40−50% over the same wavelength range. In addition, a slightly improved IPCE curve of the N-Cdot-TiO_2 NWs is observed in the visible range of 400−430 nm (Figure 3b, inset), in good accord with the UV−vis spectra of the N-Cdots (Supporting Information Figure S3). These results suggest that the much improved photoactivity of the N-Cdot-TiO_2 NWs is mainly attributed to the enhanced light absorption and charge carrier

transfer of N-Cdots functionalized to TiO_2 NW surface, similar to the previous report of the photosensitization of TiO_2 by pure Cdots.[30]

Before the detection of S^{2-}, the N-Cdot-TiO_2 NW sensor is set to the "PEC-off" state by soaking the N-Cdot-TiO_2 NW sensor into a Cu^{2+} solution, which leads to a substantial photocurrent decrease of the N-Cdot-TiO_2 NWs to almost the same level as the pristine TiO_2 NWs (Figure 3a, blue curve), suggesting the quenching of the charge transfer from N-Cdots to TiO_2 NWs. The real-time sensing experiments of S^{2-} are then carried out under the same sunlight illumination, with a small applied bias of 0 V vs Ag/AgCl (or 0.6 V vs RHE) to minimize the interference of other reductive species potentially coexisting in the solution. Upon the successive addition of S^{2-} at intervals with a final S^{2-} concentration increase of 10 and 100 nM in the PEC cell each time, well-defined steps of photocurrent increase are observed (Figure 3c). The increase of the photocurrent level is attributed to the binding of S^{2-} to Cu^{2+}, which gradually recovers the photocurrent to the original level of the N-Cdot-TiO_2 NWs, that is, the "PEC-on" state. By removing CuS and unreacted Cu^{2+} from the N-Cdot-TiO_2 NWs, this on/off cycle can be repeated for over 50 times, with ~80% of the initial photocurrent response maintained (Figure 3d). This robust sensing performance and long-term function stability of the N-Cdot-TiO_2 NW PEC sensors is attributed to the stable structures and optoelectronic performances of N-Cdots and TiO_2 NWs, as well as their strong chemical binding.

The mechanism of the influence of N-Cdots on TiO_2 is further illustrated by studying the charge transfer process between the Cdots and TiO_2. As displayed in the TEM images, Cdots or N-Cdots are directly bound to TiO_2 NW surface. Because Cdots are essentially composed of graphene sheets, a single graphene layer on TiO_2 surface is used to model the interface between the Cdot and TiO_2 lattice (Figure 4a). To understand the mechanism of fluorescence intensity change of Cdots with various nitrogen doping, First Principle calculations of optical properties for different nitrogen doping concentrations in an arbitrary defined Cdot ($C_{150}H_{30}$) are carried out.
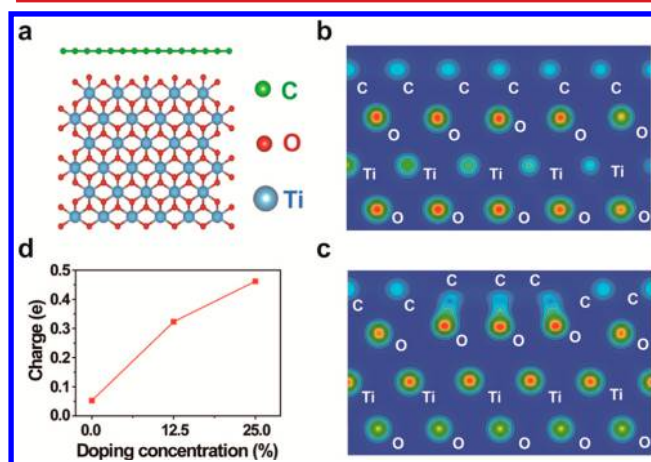

Figure 4. (a) Structure model for computational simulation of the interface of single-layer Cdots and rutile TiO_2 (100) surface. The green, red, and blue spheres represent C, O, and Ti ions/atoms, respectively. (b) Contour plots of total charge density of single-layer Cdot-TiO_2 interface in the (100) plane. (c) Contour plot of total charge density of N-doped single-layer Cdot-TiO_2 interface in the (100) plane. (d) The amount of charge transferred from N-doped single-layer Cdots to TiO_2 with different doping concentrations.

The absorption coefficient is calculated on the basis of the dielectric functions (Supporting Information Figure S8). Although the First Principle calculation applied here is a kind of ground state calculation, and the local density approximation (LDA) usually underestimates the band gap,[41] this simulation provides a semiquantitative trend of band gap size with respect to the nitrogen doping. With the increase of the nitrogen doping concentration, the Cdot shows increased absorption coefficient, consistent with the aforementioned UV−vis absorption spectra.

To study the effect of the N-doping, 12.5% and 25% of carbon atoms in the carbon layer are randomly substituted by nitrogen atoms, respectively. Structure optimization is performed for the carbon−TiO$_2$ interface system using the conjugate gradient method. The equilibrium distance between the graphene layer and the top atomic layer of TiO$_2$ is obtained as 1.099 Å for pure carbon layer and 1.148 and 1.496 Å for 12.5% and 25% N-doped carbon layers, respectively. The average charge transfer is analyzed on the basis of the Bader method.[38] For the pure carbon−TiO$_2$ interface, an average charge transfer of ~0.05 electron per carbon atom is observed from the pure carbon layer to TiO$_2$ (Figure 4b). In contrast, 0.32 and 0.46 electrons per carbon atom are obtained from the 12.5% and 25% N-doped carbon layer to TiO$_2$, respectively (Figure 4c, d). The spontaneous interfacial charge transfer can be attributed to the large difference in work functions between carbon and TiO$_2$.[39,40] For N-doped Cdots, the charge transfer rate is enhanced dramatically, due to the electron donation from the doped N atoms. Moreover, the charge carrier densities are measured by the electrochemical impedance spectroscopy. The N-Cdot-TiO$_2$ NWs show much smaller slopes in the Mott−Schottky plots, indicating significantly higher charge carrier densities compared with the Cdot-TiO$_2$ NWs and pristine TiO$_2$ NWs (Supporting Information Figure S9).

Furthermore, the band alignment relative to the vacuum level for TiO$_2$, graphene, 25% N-doped graphene, and Cu^{2+} is exhibited (Supporting Information Figure S10) either based on the simulation or obtained from references.[41] The valence band maximum (VBM) of TiO$_2$ and graphene are found to be 7.88 and 5.16 eV below the vacuum energy level. The offsets of graphene and 25% N-doped graphene are calculated using the standard computation approach.[42] The VBM of the graphene and N-doped graphene are close to each other (0.14 eV). The spontaneous interfacial charge transfer can be explained by the large difference between the band alignments of TiO$_2$ and graphene or N-doped graphene. Because the difference of VBM between graphene and N-doped graphene is small, the enhancement of charge transfer is attributed to the charge doping. In addition, because the energy level of Cu^{2+} is higher than VBM of graphene and lower than the conduction band minimum (CBM) of graphene, the quenching of the energy transfer by Cu^{2+} can also be explained.

Finally, the capability of using the N-Cdot-TiO$_2$ NW sensor for the PEC recording of H$_2$S release from living cells is demonstrated. H9c2 cardiac myoblasts are directly cultured on top of vertically aligned N-Cdot-TiO$_2$ NW arrays. After reaching the growth confluence, SEM images of the fixed cells show that the H9c2 cardiac myoblasts preserve normal morphologies and tight junctions contacting to the NW interfaces (Figure 5a). The spreading of H9c2 cardiac myoblasts on the tips of NW arrays suggest excellent cell−NW interactions (Figure 5b), as that reported previously in other cell−NW interfaces.[43] The normal morphologies, active
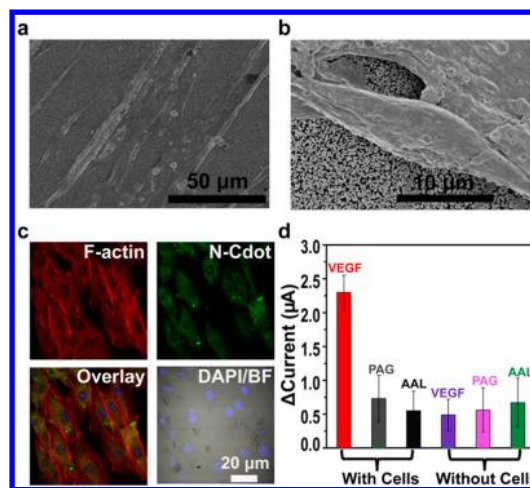
Figure 5. N-Cdot-TiO$_2$ NW/cardic myoblast cell interface and PEC sensing. The size of the active sensor area was 0.02−0.06 cm^2, defined by epoxy sealing. (a, b) SEM images of H9c2 cells grown on top of N-Cdot-TiO$_2$ NW arrays. (c) Confocal fluorescence microscope images of proliferation of H9c2 cells grown on N-Cdot-TiO$_2$ NW arrays. Cells were stained to visualize F-actins (red), cytoplasm (green), and nuclei (blue). (d) Summary of PEC photocurrent changes recorded from a N-Cdot-TiO$_2$ NW sensor interfacing with H9c2 cells at 0 V vs Ag/AgCl under sunlight illumination. Different stimulation and inhibition reagents: 40 ng/mL VEGF stimulation (red bar), 100 μM PAG for 10 min before VEGF stimulation (gray bar), and 30 μM AL-993 for 40 min before VEGF stimulation (black bar). Another N-Cdot-TiO$_2$ NW sensor without cell culture is displayed as a control under similar reagent additions.

cell functions and proliferation of living H9c2 cardiac myoblasts are clearly exhibited by the fluorescence imaging (Figure 5c), in which F-actins, cytoplasm, and nuclei of the cells are labeled by phalloidin-tetramethylrhodamine B isothiocyanate (red), N-Cdots (green), and 4′,6-diamidino-2-phenylindole dihydrochloride (DAPI, blue). The cell viability is retained at >95% and >80% after 24 and 96 h growth on the NW arrays, respectively, thus suggesting that low cytotoxicity of the NW sensor platform for cell culture (Supporting Information Figure S11).

The PEC recording of H$_2$S at the interface between N-Cdot-TiO$_2$ NWs and cardiac myoblast cells is further investigated by the stimulation of H9c2 cardiac myoblasts using VEGF, which is a key regulator of physiological angiogenesis during embryogenesis, skeletal growth, and reproductive functions, as well as an effective stimulator for cellular H$_2$S regulation.[44] For the stimulation test, the PEC photocurrent of N-Cdot-TiO$_2$ NWs interfacing with H9c2 cardiac myoblasts are directly measured at 0 V vs Ag/AgCl under 100 mA cm^{-2} of simulated sunlight. VEGF injections with final concentration increases of ~40 ng nL^{-1} each time is added into the cell culture over the sensor array. A substantial increase of photocurrent of 2.3 μA is obtained within 3 min from the N-Cdot-TiO$_2$ NW photoanodes (Figure 5d, red bar), suggesting the generation of H$_2$S from the cardiac myoblast cells. Furthermore, the dose-dependent effect of VEGF on their recorded PEC sensor signals are investigated, which shows an increase of photocurrent change with the VEGF concentration range from 10−40 ng/mL (Supporting Information Figure S12). The process of the VEGF stimulation is further confirmed by the inhibition experiments, in which the NW sensors/cells are preincubated with DL-propargylglycine (PAG) before the addition of VEGF. Under the otherwise same conditions, the photocurrent of the

N-Cdot-TiO$_2$ NW photoanode interfacing with living H9c2 cardiac myoblasts, preincubated with PAG, does not show observable amperometric responses upon the additions of VEGF (Figure 5d, gray bar). This result is consistent with a recent report that PAG inhibits the function of cystathionine γ-lyase (CSE), an essential H$_2$S-producing enzyme in vasculature.[45,46] Similarly, preincubation of 2-(pyridin-4-ylmethyl)-amino-N-(3-(trifluoromethyl)phenyl)benzamide (AAL-993) also produces negligible PEC current increase upon the VEGF stimulation (Figure 5d, black bar), in good accord with the fact that AAL-993 can effectively inhibit the tyrosine kinase domain of VEGFR2 and, thus, the VEGF-triggered H$_2$S generation.[43] In comparison, the N-Cdot-TiO$_2$ NW photoanodes without interfacing to H9c2 cardiac myoblasts do not show signals to either the additions of VEGF or any PAG or AAL-993 injections before the VEGF stimulation. Taken together, these results indicate that the PEC current increase of the N-Cdot-TiO$_2$ NW sensor is attributed to the generation of H$_2$S via different cellular pathways and further suggests the potential use of the highly sensitive N-Cdot-TiO$_2$ NW photoanodes for PEC recording of cellular functions.

The synthesis of N-doped Cdots by the microwave-assisted pyrolysis includes the decomposition of anhydrous citric acid and melamine, followed by the surface passivation of the amine groups of AEAPMS with the carboxyl groups derived from the pyrolyzed species. The microwave-assisted approaches allow for high reaction selectivity, rapid temperature elevation, and homogeneous heating,[47] thus enabling the in situ synthesis of N-doped Cdots in our work. The functional groups of organosilanes provide solvent environment with high boiling point for surface passivation, as well as for chemical coupling on the Cdot surface. The high quantum yield of the obtained N-Cdots should be attributed to their high photoabsorption and conversion efficiency, as well as the N-doping by pyrolysis of melamine.[35] Furthermore, the N-doping leads to a much enhanced and stable fluorescence compared to undoped Cdots, allowing for more efficient charge transfer toward TiO$_2$ NWs and thus the photocurrent increase.

On the basis of the results above, an interfacial charge carrier transfer and tuning mechanism is proposed to illustrate the N-Cdot-TiO$_2$ NW PEC sensors. N-Cdots serve as fluorophores and sensitizers for TiO$_2$ NWs. The photogenerated electrons are injected into the conduction band of the TiO$_2$ NWs in contact and subsequently transported along the axial direction of TiO$_2$ NWs to the counter electrode for the water reduction. Meanwhile, the photogenerated holes in both the N-Cdots and TiO$_2$ NWs are transferred into the photoanode surface to oxidize water. This electron transfer pathway between the N-Cdots and TiO$_2$ NWs is quenched by the existence of Cu^{2+} in electrolyte solution, which can be attributed to the competition and transfer of photogenerated electrons from the excited states of N-Cdots to the d orbitals of Cu^{2+},[48] and thus, the photocurrent drops to the level of pristine TiO$_2$ NWs (the "PEC-off" state). As H9c2 cardiac myoblasts are directly grown on and closely contacted to the N-Cdot-TiO$_2$ NW arrays, the introduction of VEGF can effectively excite H9c2 cardiac myoblasts to produce H$_2$S, which leads to CuS formation due to the high binding constants between S^{2-} and Cu^{2+} ions. The process reduces the local concentration of Cu^{2+} near the PEC sensor surface; hence, the transfer of photogenerated electrons is reinstated and the photocurrent is increased to the "PEC-on" stage. This sensing mechanism utilizes Cu^{2+} to tune the enhancement and reduction of the charge transfer between N-Cdots and TiO$_2$ NWs, allowing for detection of H$_2$S. Thus, by directly interfacing with H9c2 cardiac myoblasts, the N-Cdot-TiO$_2$ NW PEC sensor can be used to investigate possible pathways that lead to the H$_2$S generation upon the VEGF stimulation of living cells.

Moreover, the PEC conversion-based sensing platform of the N-Cdot-TiO$_2$ NWs offers several unique features. First, the use of sunlight (or other low-intensity illumination) can eventually waive the need of laser or external electric field for signal stimulation and reduce possible side electrochemical reactions and background noise. Second, the interfacial molecule competition-based charge transfer mechanism design and the PEC tuning approach can be extended to a variety of other molecule detections using the chemically functionalized N-Cdot-TiO$_2$ NWs. Last, the NW-based living cell interface can also be used for real-time recording and analyzing of production and variation of cellular trace molecules under various stimulations.

In summary, we have developed a microwave-assisted solvothermal synthesis for the nitrogen-doped carbon nanodots and chemical functionalization on the surface of TiO$_2$ NW arrays. The obtained N-Cdot-TiO$_2$ NW photoanodes provide much enhanced photocurrent densities compared to pristine TiO$_2$ NWs, which is attributed to the injection of photo-generated electrons from the N-Cdots to the TiO$_2$ NWs. DFT simulation reveals that the charge transfer efficiency between the N-Cdots and TiO$_2$ NWs is substantially enhanced with the increase of the N-doping ratio between 0 and 25%. This charge carrier transfer efficiency can be quenched by the existence of Cu^{2+} in the solution, which reduces the PEC current to a lower level similar to the pristine TiO$_2$ NWs. This interfacial charge transfer and tuning mechanism allows for a unique and sensitive modality for real-time probing of physiological levels of H$_2$S or S^{2-} ions in the solution. The PEC current is recovered upon the addition of S^{2-}, with the lowest detectable S^{2-} concentration of 10 nM. Moreover, by direct culturing and interfacing of H9c2 cardiac myoblasts on the N-Cdot/TiO$_2$ NW arrays, the pathways of cellular stimulation by VEGF as well as the inhibition are studied based on the real-time recording of the cellular H$_2$S generation. This low-cost, sensitive, and stable N-Cdot-NWs/living cell interface can open up new avenues to the Cdot-based, as well as other semiconductor-based, NWs/living cell interface. Further understanding of the N-Cdot-TiO$_2$ NW/cell interface will ultimately lead to better realization of the PEC nanobio interactions and the rationally guided design of future tools for life sciences.

■ ASSOCIATED CONTENT

Ⓢ Supporting Information

Details of methods, supporting figures, including AFM topography, XPS spectra, UV−vis spectra, photographs, growth inhibition results, elemental mapping, FTIR spectra, absorption coefficients, Mott−Schottky polts, band alignment, cytotoxicity evaluation, and dose-related effects, and related references. This material is available free of charge via the Internet at http://pubs.acs.org.

■ AUTHOR INFORMATION

Corresponding Authors

*E-mail: gfzheng@fudan.edu.cn (G.Z.).
*E-mail: xggong@fudan.edu.cn (X.G.).

■ REFERENCES

(1) Jiang, S.; Cheng, R.; Wang, X.; Xue, T.; Liu, Y.; Nel, A.; Huang, Y.; Duan, X. *Nat. Commun.* **2013**, *4*, 2225.

(2) Thoi, V. S.; Kornienko, N.; Margarit, C. G.; Yang, P.; Chang, C. J. *J. Am. Chem. Soc.* **2013**, *135*, 14413−14424.

(3) Liu, J.; Yee, K. K.; Lo, K. K. W.; Zhang, K. Y.; To, W. P.; Che, C. M.; Xu, Z. *J. Am. Chem. Soc.* **2014**, *136*, 2818−2824.

(4) Tian, B.; Cohen-Karni, T.; Qing, Q.; Duan, X.; Xie, P.; Lieber, C. M. *Science* **2010**, *329*, 830−834.

(5) Xie, C.; Hanson, L.; Xie, W.; Lin, Z.; Cui, B.; Cui, Y. *Nano Lett.* **2010**, *10*, 4020−4024.

(6) Qing, Q.; Jiang, Z.; Xu, L.; Gao, R.; Mai, L.; Lieber, C. M. *Nat. Nanotechnol.* **2014**, *9*, 142−147.

(7) Dong, X.; Yang, C.; Zheng, D.; Mo, L.; Wang, X.; Lan, A.; Hu, F.; Chen, P.; Feng, J.; Zhang, M. *Mol. Cell. Biochem.* **2012**, *362*, 149−157.

(8) Bailey, T.; Pluth, M. *J. Am. Chem. Soc.* **2013**, *135*, 16697−16704.

(9) Yang, G.; Wu, L.; Jiang, B.; Yang, W.; Qi, J.; Cao, K.; Meng, Q.; Mustafa, A.; Mu, W.; Zhang, S.; Snyder, S.; Wang, R. *Science* **2008**, *322*, 587−590.

(10) Chen, S.; Chen, Z.; Ren, W.; Ai, H. *J. Am. Chem. Soc.* **2012**, *134*, 9589−9592.

(11) Mai, L.; Xu, L.; Gao, Q.; Han, C.; Hu, B.; Pi, Y. *Nano Lett.* **2010**, *10*, 2604−2608.

(12) Qian, Y.; Karpus, J.; Kabil, O.; Zhang, S.; Zhu, H.; Banerjee, R.; Zhao, J.; He, C. *Nat. Commun.* **2011**, *2*, 495.

(13) Chen, Y.; Zhu, C.; Yang, Z.; Chen, J.; He, Y.; Jiao, Y.; He, W.; Qiu, L.; Cen, J.; Guo, Z. *Angew. Chem., Int. Ed.* **2013**, *125*, 1732−1735.

(14) Lippert, A. R.; New, E. J.; Chang, C. J. *J. Am. Chem. Soc.* **2011**, *133*, 10078−10080.

(15) Xiong, B.; Zhou, R.; Hao, J.; Jia, Y.; He, Y.; Yeung, E. S. *Nat. Commun.* **2013**, *4*, 1708.

(16) Tang, J.; Kong, B.; Wang, Y.; Xu, M.; Wang, Y.; Wu, H.; Zheng, G. *Nano Lett.* **2013**, *13*, 5350−5354.

(17) Tang, J.; Wang, Y.; Li, J.; Da, P.; Geng, J.; Zheng, G. *J. Mater. Chem. A* **2014**, *2*, 6153−6157.

(18) Chen, D.; Zhang, H.; Li, X.; Li, J. *Anal. Chem.* **2010**, *82*, 2253−2261.

(19) Lu, W.; Wang, G.; Jin, Y.; Yao, X.; Hu, J.; Li, J. *Appl. Phys. Lett.* **2006**, *89*, 263902.

(20) Shi, J.; Hara, Y.; Sun, C.; Anderson, M. A.; Wang, X. *Nano Lett.* **2011**, *11*, 3413−3419.

(21) Mayer, M. T.; Lin, Y.; Yuan, G.; Wang, D. *Acc. Chem. Res.* **2013**, *46*, 1558−1566.

(22) Wang, Y.; Zhang, Y.; Tang, J.; Wu, H.; Xu, M.; Peng, Z.; Gong, X. G.; Zheng, G. *ACS Nano* **2013**, *7*, 9375−9383.

(23) Murdoch, M.; Waterhouse, G.; Nadeem, M.; Metson, J.; Keane, M.; Howe, R.; Llorca, J.; Idriss, H. *Nat. Chem.* **2011**, *3*, 489−492.

(24) Crossland, E. J.; Noel, N.; Sivaram, V.; Leijtens, T.; Alexander-Webber, J. A.; Snaith, H. J. *Nature* **2013**, *495*, 215−219.

(25) Hwang, Y. J.; Hahn, C.; Liu, B.; Yang, P. *ACS Nano* **2012**, *6*, 5060−5069.

(26) Wang, G.; Wang, H.; Ling, Y.; Tang, Y.; Yang, X.; Fitzmorris, R. C.; Wang, C.; Zhang, J. Z.; Li, Y. *Nano Lett.* **2011**, *11*, 3026−3033.

(27) Liu, B.; Chen, H. M.; Liu, C.; Andrews, S. C.; Hahn, C.; Yang, P. *J. Am. Chem. Soc.* **2013**, *135*, 9995−9998.

(28) Sun, W. T.; Yu, Y.; Pan, H. Y.; Gao, X. F.; Chen, Q.; Peng, L. M. *J. Am. Chem. Soc.* **2008**, *130*, 1124−1125.

(29) Hensel, J.; Wang, G.; Li, Y.; Zhang, J. Z. *Nano Lett.* **2010**, *10*, 478−483.

(30) Zhang, X.; Huang, H.; Liu, J.; Liu, Y.; Kang, Z. *J. Mater. Chem. A* **2013**, *1*, 11529−11533.

(31) Sun, M.; Ma, X.; Chen, X.; Sun, Y.; Cui, X.; Lin, Y. *RSC Adv.* **2014**, *4*, 1120−1127.

(32) Zhang, X.; Wang, F.; Huang, H.; Li, H.; Han, X.; Liu, Y.; Kang, Z. *Nanoscale* **2013**, *5*, 2274−2278.

(33) Tang, J.; Kong, B.; Wu, H.; Xu, M.; Wang, Y.; Wang, Y.; Zhao, D.; Zheng, G. *Adv. Mater.* **2013**, *25*, 6569−6574.

(34) Dong, Y.; Pang, H.; Yang, H. B.; Guo, C.; Shao, J.; Chi, Y.; Li, C. M.; Yu, T. *Angew. Chem., Int. Ed.* **2013**, *52*, 7800−7804.

(35) Li, W.; Zhang, Z.; Kong, B.; Feng, S.; Wang, J.; Wang, L.; Yang, J.; Zhang, F.; Wu, P.; Zhao, D. *Angew. Chem., Int. Ed.* **2013**, *52*, 8151−8155.

(36) Xie, Z.; Wang, F.; Liu, C. y. *Adv. Mater.* **2012**, *24*, 1716−1721.

(37) Zhu, A.; Qu, Q.; Shao, X.; Kong, B.; Tian, Y. *Angew. Chem., Int. Ed.* **2012**, *124*, 7297−7301.

(38) Tang, W.; Sanville, E.; Henkelman, G. *J. Phys.: Condens. Matter* **2009**, *21*, 084204.

(39) Gao, H.; Li, X.; Lv, J.; Liu, G. *J. Phys. Chem.* **2013**, *117*, 16022−16027.

(40) Du, A.; Ng, Y. H.; Bell, N. J.; Zhu, Z.; Amal, R.; Smith, S. C. *J. Phys. Chem. Lett.* **2011**, *2*, 894−899.

(41) Onida, G.; Reining, L.; Rubio, A. *Rev. Mod. Phys.* **2002**, *74*, 601−659.

(42) Wei, S.; Zunger, A. *Appl. Phys. Lett.* **1998**, *72*, 2011.

(43) Xie, C.; Lin, Z.; Hanson, L.; Cui, Y.; Cui, B. *Nat. Nanotechnol.* **2012**, *7*, 185−190.

(44) Lin, V. S.; Lippert, A. R.; Chang, C. J. *Proc. Natl. Acad. Sci. U. S. A.* **2013**, *110*, 7131−7135.

(45) Li, L.; Bhatia, M.; Zhu, Y. Z.; Zhu, Y. C.; Ramnath, R. D.; Wang, Z.; Anuar, F. B. M.; Whiteman, M.; Salto-Tellez, M.; Moore, P. K. *FASEB J.* **2005**, *19*, 1196−1198.

(46) Shatalin, K.; Shatalina, E.; Mironov, A.; Nudler, E. *Science* **2011**, *334*, 986−990.

(47) Coffin, R. C.; Peet, J.; Rogers, J.; Bazan, G. C. *Nat. Chem.* **2009**, *1*, 657−661.

(48) Hou, X.; Zeng, F.; Du, F.; Wu, S. *Nanotechnology* **2013**, *24*, 335502.